AGU PUBLICATIONS

JGR

Journal of Geophysical Research: Atmospheres

RESEARCH ARTICLE

10.1002/2017JD027309

Key Points:

- New AOT estimation technique that improves the performance of low-cost Sun photometers for distributed measurements at a metropolitan scale
- Aerosol spatial distribution and dynamics show that at least in Santiago basin requires much denser measurement network
- Low-cost Sun photometers can be used to study atmospheric dynamics by using aerosols as tracers

Supporting Information:

- Supporting Information S1

Correspondence to:
M. Díaz,
mdiazq@ing.uchile.cl

Citation:
Toledo, F., Garrido, C., Díaz, M., Rondanelli, R., Jorquera, S., & Valdivieso, P. (2018). AOT retrieval procedure for distributed measurements with low-cost Sun photometers. *Journal of Geophysical Research: Atmospheres*, *123*, 1113–1131. https://doi.org/10.1002/2017JD027309

Received 14 JUL 2017
Accepted 16 NOV 2017
Accepted article online 7 DEC 2017
Published online 23 JAN 2018

AOT Retrieval Procedure for Distributed Measurements With Low-Cost Sun Photometers

F. Toledo[1,2], **C. Garrido**[1,2,3], **M. Díaz**[1,2], **R. Rondanelli**[2,4,5], **S. Jorquera**[2,3], and **P. Valdivieso**[3,4]

[1]Electrical Engineering Department, Faculty of Physical and Mathematical Sciences, University of Chile, Santiago, Chile, [2]Space and Planetary Exploration Laboratory, Faculty of Physical and Mathematical Sciences, University of Chile, Santiago, Chile, [3]Department of Mechanical Engineering, Faculty of Physical and Mathematical Sciences, University of Chile, Santiago, Chile, [4]Department of Geophysics, Faculty of Physical and Mathematical Sciences, University of Chile, Santiago, Chile, [5]Center for Climate and Resilience Research, University of Chile, Santiago,Chile

Abstract We propose a new application of inexpensive light-emitting diode (LED)-based Sun photometers, consisting of measuring the aerosol optical thickness (AOT) with high resolution within metropolitan scales. Previously, these instruments have been used at continental scales by the GLOBE program, but this extension is already covered by more expensive and higher-precision instruments of the AERONET global network. For this we built an open source two-channeled LED-based Sun photometer based on previous developments, with improvements in the hardware, software, and modifications on the calibration procedure. Among these we highlight the use of MODTRAN to characterize the effect introduced by using LED sensors in the AOT retrieval, an open design available for the scientific community and a calibration procedure that takes advantage of a CIMEL Sun photometer located within the city, enables the intercomparison of several LED Sun photometers with a common reference. We estimated the root-mean-square error in the AOT retrieved by the prototypes as 0.006 at the 564 nm and 0.009 at the 408 nm. This error is way under the magnitude of the AOT daily cycle variability measured by us in our campaigns, even for distances closer than 15 km. In addition to inner city campaigns, we also show aerosol-tracing applications by measuring AOT variations from the city of Santiago to the Andes glaciers. Measuring AOT at high spatial resolution in urban areas can improve our understanding of urban scale aerosol circulation, providing information for solar energy planning, health policies, and climatological studies, among others.

1. Introduction

Aerosols have a relevant impact in human health as well as climate through changes in radiative process and in cloud formation. This paramount role has motivated the development of measurement systems. Some of these systems are space-based (e.g., MODIS, CALIPSO) and others are networks of ground-based instruments (e.g., AERONET, Holben et al., 1998). One of the most used ground-based instruments for aerosol monitoring is the Sun photometer.

Volz (1959) introduced the first handheld ground-based atmospheric aerosol measurements using Sun photometry. Technology has changed substantially since then, allowing portability and automation of field instruments. The CIMEL and PREDE (French and Japanese manufacturers, respectively) are current examples of commercial high-precision Sun photometers. The AERONET (Holben et al., 1998) is an aerosol-monitoring network composed by these high-precision Sun photometers. The network was developed in the late 1990s by NASA to encourage measurements at a global scale with the aim of measuring Aerosol Optical Thickness (AOT) and study its impact on global climate. The average distance between each instrument in this network is currently above 50 km (excluding the oceans).

Besides this effort, in the early 1990s a pioneering work was carried out to develop inexpensive handheld Sun photometers based on light-emitting diodes (LED) (Hauser et al., 1995; Mims III, 1992). These low-cost Sun photometers have also been used at a global collaboration for education and science in the GLOBE initiative (Butler & MacGregor, 2003). In more recent efforts this low-cost Sun photometer type has been used to study aerosol seasonal variations at regional scales in China (Wang et al., 2011; Xin et al., 2007).

AERONET, GLOBE, and Hazemeter networks improve global/regional coverage, and alongside satellite observations from instruments such as MODIS, it is possible to get good quality of AOT measurements at a global/regional scale. However, at urban locations, the surface characteristics can change drastically over short distances (in the order of kilometers). This introduces difficulties in the estimation of the AOT behavior within cities using satellite measurements, since their retrieval algorithms rely on the estimation of surface properties such as the reflectivity. For instance, standard MODIS AOT products are found to have significant biases when compared to ground-based measurements due to difficulties in accounting for changes of the surface reflectivity (Escribano et al., 2014).

Higher spatial resolution AOT products such as MAIAC (Lyapustin et al., 2011) introduce improvements in the retrieval algorithms using MODIS radiances, but the information they provide is still limited to two overpasses each day. MAIAC measurements over Santiago of Chile suggest that the aerosol dynamics inside the city has a rich behavior that cannot be accounted for with a single Aeronet station. Therefore, we explore this preliminary finding by using low-cost LED-based Sun photometers like those proposed by Mims III (1992). Nevertheless, the accuracy, reliability, and fidelity of the AOT measurements obtained with these low-cost instrument has to be improved.

Ideally, to improve the AOT characterization on urban areas one would increase the spatial density by using a large number of high-quality robotic Sun photometers, but that would be prohibitively expensive, especially in developing countries. For example, there is only one CIMEL located in the city of Santiago of Chile. This prevents the study of the aerosols dynamics with higher spatial resolution at a metropolitan scale. On the other hand, improving the AOT measurement resolution by only using low-cost LED-based Sun photometers may introduce difficulties in the error quantification and in the fidelity of the measurements.

In this work, we propose improvements in hardware, software, and data processing (AOT estimation procedure) to the Sun photometer developed in GLOBE, which are described in detail in the supporting information of this article. Additionally, we propose a method consisting of using inexpensive LED-based Sun photometers alongside commercial Sun photometers such as the CIMEL to increase the characterization of the AOT behavior both in spatial and temporal scales. In our proposed procedure the CIMEL is used as a reference instrument that provides a common base that we can use to enable the intercomparison of data retrieved with low-cost LED-based Sun photometers.

This joint use adds information about the local behavior of aerosols occurring in an area of much smaller scale than that proposed for both the AERONET and GLOBE systems (as exemplified in our campaigns). Model-based spatial resolution improvements have also been proposed (Li et al., 2015) as well as forthcoming geostationary satellite estimations of AOT (see, e.g., Superczynski et al., 2017). These methods also benefit from denser ground measurements since they will need in situ calibration and validation sources with well-characterized uncertainties.

This work is organized as follow: in section 2 we describe the instrument development, in section 3 we describe the evaluation of LED diodes as AOT sensors, in section 4 the calibration procedure is presented, in section 5 we present the results of two field campaigns using the developed instruments, and in section 6 we discuss the main conclusions of this work.

2. The Instrument Prototype

The sun photometer presented in this section is a revised and improved version of the Sun photometer developed by Brooks and Mims (2001). It still uses the same principle published by Mims III (1992), with LEDs as selective band sensors but includes technological improvements and changes in the licensing. All components are integrated into an embedded system, with an electronic interface, internal clock, sensors, data memory, and battery. This provides robustness to the instrument due to the protection of its internal elements and simplifies the operation, in a similar way provided by other handheld Sun photometers (MICROTOPS, CALITOO). Additionally, this instrument not only measures air temperature, it also registers the atmospheric pressure to enable a more accurate estimation of the Rayleigh scattering effect (see section 2.3). The last upgrade is the use of brighter LEDs as sensors. These LEDs have a more intense response to light when compared with those used by Brooks and Mims (2001), which increases the signal to noise ratio and reduce the impact of the LEDs dark current (more details in section 2.1.1).

The other main area of improvement, which is what sets this prototype apart, is the licensing and the possibilities of replication. By choosing Open Source licenses, prioritizing the use of consumer electronics and

Table 1
Components and Materials

Components	Material
Control panel	ABS
Solar aim	ABS
Tripod adapter	ABS
External cover	PVC
Electrical components	
LED sensor PCB	
Armaduino[a]	
MicroSD Data Logger	
DS1307 Real Time Clock Shield	
BMP180 Pressure and Temperature sensor	
LED Sensor	
9V Battery	

[a] A local version of Arduino Uno.

elaborating adequate documentation including blueprints and building instructions, we believe it is possible for anyone with the appropriate equipment to make, audit, or even improve these Sun photometers. This is encouraged by sharing this information at the GitHub repository https://github.com/FelipeToledo/DIY-SunPhotometer-UChile.

The instrument design can be further divided in three main blocks: The electronic, mechanical, and software (estimation model) subsystems. In the following sections we describe each of these subsystems, including the motivations behind the design. The main electronic and mechanical components of this low-cost open hardware-software Sun photometer are summarized in Table 1 and shown in Figure 1.

2.1. Electronic Subsystem

2.1.1. LED Sensor

One of the main limitations of using LEDs as sensors is the relatively broad spectral response function. CIMEL Sun photometers, for instance, use filters with FWHM of 10 nm, while our instrument has a spectral band of approximately 100 nm. The normalized response function of the two sensors chosen for the prototypes can be seen on Figure 2. To obtain these curves, each LED was exposed to a sliding wavelength monochromatic light source generated by an Oriel Instruments 77200 Monochromator with a Xenon lamp of 1000 (W) LOT Oriel.

The spectral width of the monochromatic beam was less than 5 (nm), enabling us to characterize with good detail the response of the LEDs in function of the wavelength. Figure 2 shows the LEDs response curves, alongside the absorption lines of water vapor and ozone.

Compared with Brooks and Mims (2001) LEDs, the LEDs selected for our Sun photometer have two major differences:

1. The luminous intensity of the LEDs. Brooks and Mims (2001) instrument uses two LEDs with a luminosity between 2.4 (mcd) and 70 (mcd), while ours have a luminosity of 7,150 (mcd) for the yellow and 8,000 (mcd) for the blue channel. As semiconductors, our LEDs are more efficient converting electrical energy in light, which translates into higher output currents when used as photodiodes.
2. We used blue and yellow LEDs with AOT equivalent wavelengths of 408 and 564 (nm), respectively (see section 2.3). On the other hand, Brooks and Mims (2001) use green and red LEDs with AOT equivalent wavelengths of approximately 505 and 625 (nm), respectively.

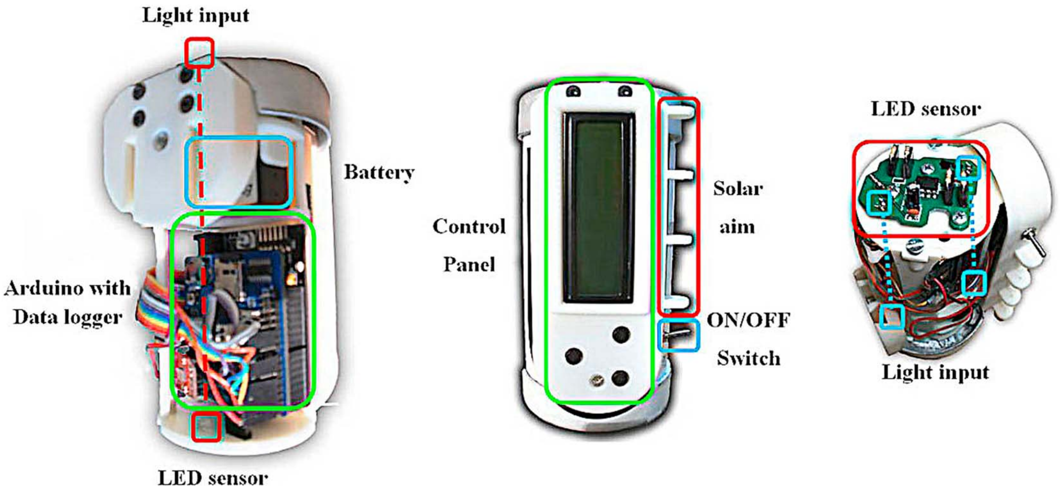

Figure 1. Sun photometer prototype. The left picture illustrates the control system, then at the middle the external cover, and to the right the LED sensor and light input.

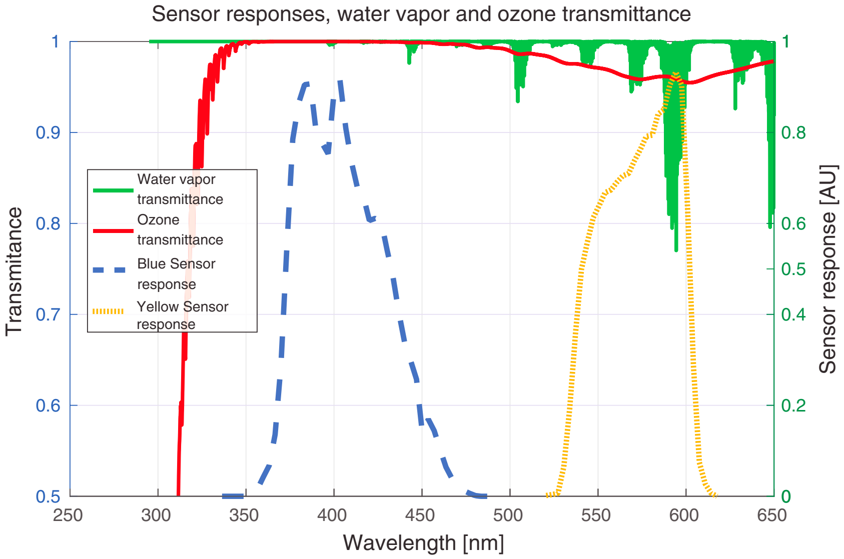

Figure 2. Blue and yellow LEDs relative response superposed to the H_2O and O_3 absorption lines. After checking the main absorption bands it was discovered that the yellow sensor response curve is coincident with water vapor and ozone absorption regions, while the curve of the blue LED is free from these effects. To obtain the LED wavelength response, each LED was exposed to a sliding wavelength monochromatic light source generated by an Oriel Instruments 77200 Monochromator with a Xenon lamp of 1,000 [W] LOT Oriel.

When the LEDs receive light from the Sun they generate a small current proportional to its intensity. This current is amplified and converted to a proportional voltage. Then, this output voltage is measured using the Analog to Digital Converter (ADC) included in an Arduino platform, a popular open hardware system. The ADC provides a 10 bit resolution for a voltage range that spans from 0 to 5 (V) and provides a sampling rate 400 samples per second.

To check for possible biases introduced by the dark current of the photodiodes, we used a multimeter to measure the output voltage of each sensor when covered from light sources. The resulting voltage output is around 0.7–0.8 (mV) and 1.2–1.7 (mV) for blue and yellow sensors, respectively. In both cases the bias introduced by the dark current is lower than the resolution of the Arduino ADC (of approximately 4.9 (mV)), which implies that it is safe to neglect the dark current effect in our voltage measurements.

2.1.2. Digital Back End

The Arduino platform is also our instrument's microcontroller. This is due to its simplicity of use and low cost, which eases the development for new groups. We also incorporated a Datalogger Shield, which enables date, time, and measurement recording capabilities onto a SD memory card and a user interface, composed by an LCD screen and three buttons. The recorded data can be extracted using a serial connection located in the case, thus it is not necessary to open the instrument's case at any time.

Regarding the measurement process, AOT retrieval requires to precisely aim at the Sun. We made this process easier by using a sampling span of 14 s. By making the assumption that the output voltage of the sensors will be maximum when the Sun is directly targeted, we can choose the higher-valued sample from the 5,600 voltages converted by the ADC in this period. Therefore, the instrument does not require to point precisely to the Sun all the time, it only requires to pass over the Sun in one of these 5,600 opportunities within 14 s.

The sampling period was chosen empirically after some field testing. It proved being short enough to assume a constant AOT value but also provided enough time to obtain a direct beam power measurement from the Sun with high probability.

2.2. Mechanical Subsystem

In order to have a low-cost mechanical structure for the Sun photometer we used a combination of commercially available materials and 3-D-printed pieces.

The external case is made of a tube and PVC caps made of polyvinyl chloride (PVC). This material is resistant to sunshine, high temperatures, and moisture, which makes it ideal for protection purposes. These components are also readily available as plumbing consumables.

Field tests showed that the PVC components have a good response to the environmental conditions with no apparent deformation within a year, which is crucial to ensure a consistent collimation of the LEDs with the light input (Figure 1).

For the rest of the structure we used acrylonitrile butadiene styrene (ABS), an oil-based plastic (Stratasys, 2015). This thermoplastic can be 3-D printed, allowing the fabrication of highly customized pieces such as the ones holding the electronics in place. We printed the ABS components using a Stratasys uPrint SE plus 3-D printer.

Besides ABS we also built prototypes with 3-D components printed in polylactic acid (PLA) (Stratasys, 2017) using a Makerbot Replicator II. In comparison to ABS this thermoplastic has disadvantages related with its properties and fabrication process. PLA is a plastic manufactured from plant-based materials including corn, sugar beets, or potatoes. It makes it a biodegradable and recyclable material. Among its properties there is a higher tensile modulus (2.7 – 16 (GPa) for PLA versus 2.1 and 2.4 (GPa) for ABS) and tensile strength (50 (GPa) for PLA and between 42 and 45 (MPa) for ABS). However, PLA is more brittle and has a higher surface hardness. ABS, on the other hand, provides a better structural integrity and it is more suitable to mechanical applications.

ABS elongation at break is of 45%, which is higher than the 6% of PLA. This property makes ABS more ductile than PLA. Therefore, PLA tends to break when bent. Furthermore, PLA gets weak when continuously exposed to the Sun. After 5 days of operation, cracks were evident in exposed 3-D pieces where PLA was used.

Finally, there are technological differences in the 3-D printer available for each plastic. The uPrint prints in a closed and temperature-controlled environment, which makes the ABS fabrication more precise with a resolution in the order of tenths of millimeters, while the Makerbot pieces had an error in the order of a few millimeters (without an exhaustive calibration and environmental control). This difference proved relevant for the pieces that granted the collimator.

The parts were developed selecting only from these two types of materials since they are the most used and easily found in digital fabrication hubs.

2.3. Software Subsystem: Aerosol Estimation Algorithm

AOT is a physical quantity proportional to the extinction of monochromatic light traveling through the atmosphere due to the presence of aerosols. This variable can be measured indirectly from the direct solar radiation attenuated at a given wavelength.

To estimate AOT for each sensor we use the equivalent wavelength approximation described in (Brooks & Mims, 2001), which can be seen on equation (1).

$$\tau_a(\lambda) = \frac{\ln\left(V_0\left(\frac{R_0}{R}\right)^2\right) - \ln(V) - \tau_R(\lambda)\frac{P}{P_0}\cdot m_{\text{air}}}{m_{\text{air}}} - \tau_g(\lambda) \tag{1}$$

Parameter description:

1. λ: Wavelength of the monochromatic light beam considered ([nm).
2. V: Voltage measured by a LED photodiode in (V), which is proportional to the light power received.
3. V_0: Calibration constant. Represents the estimated sensor response in (V) for a case without atmosphere. It can be obtained from a Langley calibration (see section 4.1).
4. $\left(\frac{R_O}{R}\right)^2$: Earth-Sun distance correction. R_0 is the average Sun-Earth distance (1 in (AU)) and R is the measurement day Sun-Earth distance in (AU). This term compensates the effect of Sun distance variations in the solar constant.
5. m_{air}: Relative air mass (AM). It is a dimensionless quantity that represents the length of the atmospheric path light crosses relative to the vertical column.
6. P: Pressure at the measurement spot in (hPa).
7. P_0: Sea level pressure in (hPa).
8. $\tau_R(\lambda)$: Rayleigh optical thickness (ROT). It accounts for the extinction caused by Rayleigh scattering from air molecules (mostly nitrogen and oxygen). It can be calculated using Bucholtz (1995).

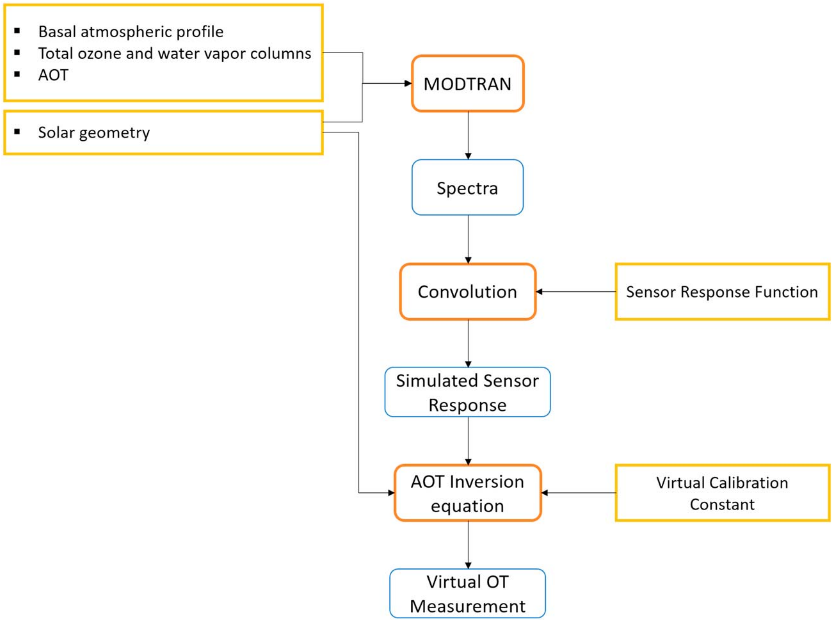

Figure 3. Virtual measurement simulation flowchart. Before obtaining Virtual OT measurements a Virtual Calibration constant must be obtained. This is done simulating Sensor Responses for different solar angles and using the Langley Plot calibration method. All the simulations were done using the U.S. Standard Atmosphere as the basal atmospheric profile (NASA, 1976).

9. $\tau_a(\lambda)$: Aerosol optical thickness (AOT). Dimensionless quantity that accounts for the light extinction caused by the aerosols, normalized to a vertical atmospheric path.
10. $\tau_g(\lambda)$: Gases optical thickness (GOT). Since LED sensors have a broad spectral response, absorption effects introduced by gases in the atmosphere are not negligible in the received signal. This term is included to clear the estimated AOT from this effect. Section 3.2 shows the methodology used to estimate this parameter.

3. Evaluation of LEDs as AOT Sensors

A potential problem that arises by using broad spectral response sensors is that the measurements might include errors introduced by atmospheric absorbing gases (see Figure 2 close to 600 nm), which is avoided by the use of narrow-filters in more expensive Sun photometers. Additionally, equation (1) corresponds to a monochromatic radiation transfer model. Therefore, the use of a sensor with a broader spectral response might introduce another error in the estimation of the AOT value. Since this might make necessary hardware modifications and/or model improvements to account for the spectral response of the sensor, we need to evaluate the impact of using sensors with broad spectral responses.

This is done by simulating virtual AOT measurements using the software MODTRAN 5.3 (Berk et al., 2006), which can be used to model the solar radiation spectrum received after the atmospheric attenuation. Taking advantage of having our LEDs characterized, we can use this tool to simulate our sensors response by following the procedure indicated in Figure 3.

Calibration constants are obtained by simulating the sensor response on atmospheres free of aerosols and absorbing gases for several solar zenith angles. This, in fact, is just the simulation of a Langley plot calibration using virtual sensor responses (explained in section 4.1).

3.1. Effect of Using Wide Sensors on AOT Estimation

In a previous study, Brooks and Mims (2001) suggested to use an equivalent AOT wavelength λ_e for each LED as a way to enable the use of equation (1), for a broadband sensor.

$$\lambda_e = \frac{\sum_i S(\lambda_i) V_{\lambda_i} \lambda_i \Delta\lambda}{\sum_i S(\lambda_i) V_{\lambda_i} \Delta\lambda}. \tag{2}$$

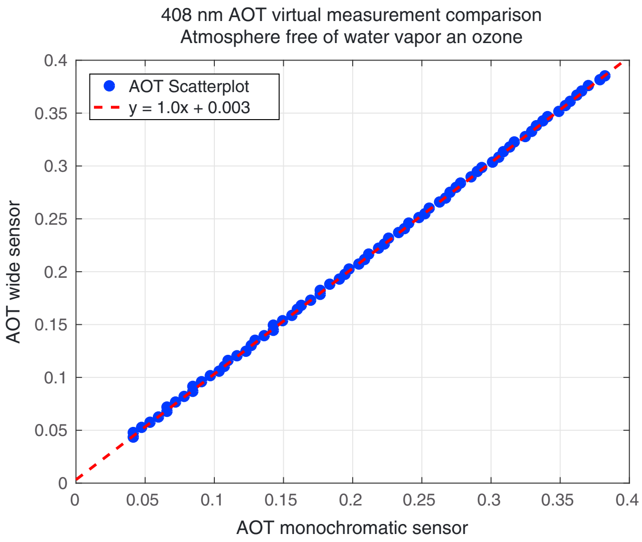

Figure 4. Comparison between the wide and narrow sensor simulated 408 nm AOT measurement. The main effect of using a wide sensor in an atmosphere with zero GOT is the appearance of a constant bias in the measurements.

Here $S(\lambda_i)$ is the top-of-the-atmosphere monochromatic irradiance and V_{λ_i} is the relative response of the sensor-associated wavelength λ_i, and $\Delta\lambda$ is the response curve sampling interval. This calculation provided average equivalent wavelengths of $\lambda_y = 564$ nm and $\lambda_b = 408$ nm for the yellow and blue LED, respectively, with variations of ± 1 nm on both channels for the three built prototypes. The procedure followed to evaluate the effect of using wide sensors over monochromatic ones in the AOT estimation can be summarized as follows:

1. Determination of equivalent wavelength for each LED response curve and its correspondent Rayleigh optical thickness (ROT) using the procedure described by Brooks and Mims (2001) with ROT coefficients published by Bucholtz (1995). An approximately monochromatic response curve (1 nm wide) is defined centered at each LED equivalent wavelength.
2. Calibration of the wide and monochromatic virtual sensors by simulating a Langley plot.
3. Perform simultaneous virtual measurements with the monochromatic and wide virtual sensors, for several AOT values.
4. Comparison of several virtual AOT measurements.

The results of this comparison are shown in Figure 4. The simulations show a strong correlation between the measurements of the broad and narrow spectral sensor, with a bias of ≈0.003 between them. This implies that the main effect of using wide sensors (in an atmosphere free of absorbing gases) is the introduction of a constant bias in the estimated AOT.

3.2. Ozone and Water Vapor Effect in the AOT Estimation

Based on MODTRAN simulations and the spectral response of our LEDs we identified water vapor and ozone as the elements that are more likely to affect our measurements, specifically on the yellow channel (see Figure 2).

To study the effect that each of these elements has we performed simulations of OT measurements for free of aerosols atmospheres with different column concentrations of a single absorbing gas.

Figure 5a shows the τ_g introduced by water vapor in the yellow sensor AOT retrieval. We obtained mean values for the error between 0.0015 and 0.012 for 0 to 3 (cm) (typical values of column water vapor in Santiago), respectively. Figure 5b shows the simulated τ_g of the ozone for column concentration between 250 and 500 (DU), and we can see that ozone attenuation is more important than the attenuation caused by the water vapor in this particular band.

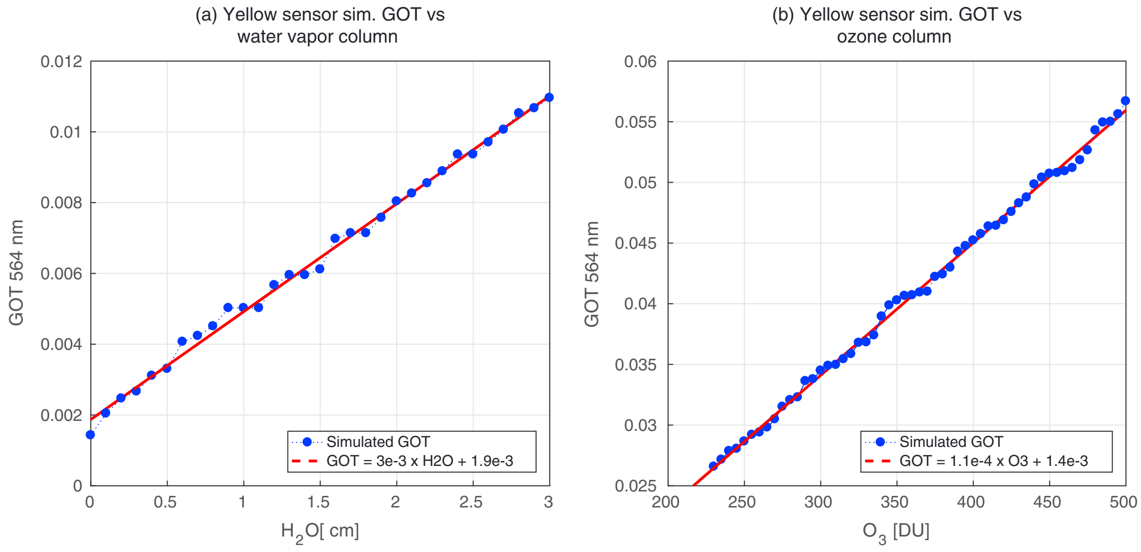

Figure 5. Simulated GOT introduced to the yellow sensor by (a) different water vapor columns and (b) stratospheric ozone concentrations.

The calculated GOT can be used to correct the yellow channel AOT estimation, using ozone and water vapor columns retrieved by using meteorological models or additional supporting instrumentation.

4. Calibration

The use of the AOT inversion equation (1) under ideal conditions only requires the knowledge of the calibration constant V_0. However, as shown in section 3.2, the error can be significant in the yellow channel due to OT contamination introduced by the atmospheric water vapor and ozone. Since the goal of this work is to improve the spatial resolution of AOT measurements, increasing the cost of the instrument by using narrow band optical filters is deemed undesirable. Therefore, we implement a data post processing to obtain a measurement uncertainty estimation and to correct assess the reliability of the measurements.

We propose a two-stage calibration. First, an estimation of the V_0 constant is obtained using Langley plot calibration. After that, the effect of the gases and sensor bias is corrected by using MODTRAN and a reference instrument. The reference instrument chosen is the *Santiago Beauchef 2* CIMEL from the AERONET monitoring network (Holben et al., 1998). It provides 2.0 quality data, which is the most reliable level according to the AERONET standards.

4.1. Langley Plot

The calibration constant V_0 is obtained by plotting the logarithm of the measured Voltage under different air mass conditions and then comparing with equation (3). This equation is a rearrangement of equation (1), assuming the equivalent wavelength approximation described previously and neglecting absorbing gases effects.

$$\ln V = \ln\left(V_0\left(\frac{R_0}{R}\right)^2\right) - \left(\tau_R\frac{P}{P_0} + \tau_a\right)m_{\text{air}} \tag{3}$$

To obtain our Sun photometer's calibration constant V_0, two Langley Plots were conducted, one during the morning and the other in the afternoon of 21 May at the Chajnantor Plateau, Atacama, Chile (4,500 m above sea level; asl). The results for the three built instruments are shown in Figure 6. Since the aerosol daily variation is unknown, the calibration constants and their variances are correlated to diminish the uncertainty in its estimation.

4.2. Measurement Correction Methodology and Error Estimation

The previous section presents the results of the experiments conducted to retrieve the calibration constant required by the AOT estimation model presented in equation (1). In this section we present the procedure we used to correct the systematic error that remains due to the effect of using wide sensors by using a reference instrument.

Since τ_R can be estimated using the site's pressure, the GOT estimation equations (4) and 5 (obtained in section 3.2) seem to be the last required element to enable the retrieval of τ_a. To obtain the gases columns, we used the ozone data provided by the ECMWF reanalysis (Dee et al., 2011) and the water vapor column retrieved by our CIMEL.

$$\text{GOT}_{\text{H}_2\text{O}} = 0.0030 \cdot \text{H}_2\text{O}\,[\text{cm}] + 0.0019 \tag{4}$$

$$\text{GOT}_{\text{O}_3} = 1.1092 \cdot 10^{-4} \cdot O_3\,[\text{DU}] + 1.353 \cdot 10^{-3}, \tag{5}$$

Although the previous procedure is quite straightforward, the comparison of data between our prototypes and our CIMEL shows that the use of this model alone still provides biased measurements. This is an expected behavior which did appear in our simulations (3.1), and may be caused at least in part by the use of wide sensors with a monochromatic transfer model.

To correct this bias effect, an intercalibration experiment is deployed, with the goal of using CIMEL measurements to correct the bias in the prototypes AOT estimation. The procedure begins by taking several measurements alongside our CIMEL. Then the prototypes data are filtered, keeping only the maximum LED sensor response within an interval of ±3 min with respect to the CIMEL sampling time. This has the objective of reducing the influence of the human operator on the data quality. After registering several simultaneous measurements, they are related using a polynomial model to obtain bias correction coefficients.

The comparisons require the interpolation of the measurements taken with the CIMEL channels to the LEDs equivalent wavelengths (Brooks & Mims, 2001). To do this, we use the Ångström exponent formula

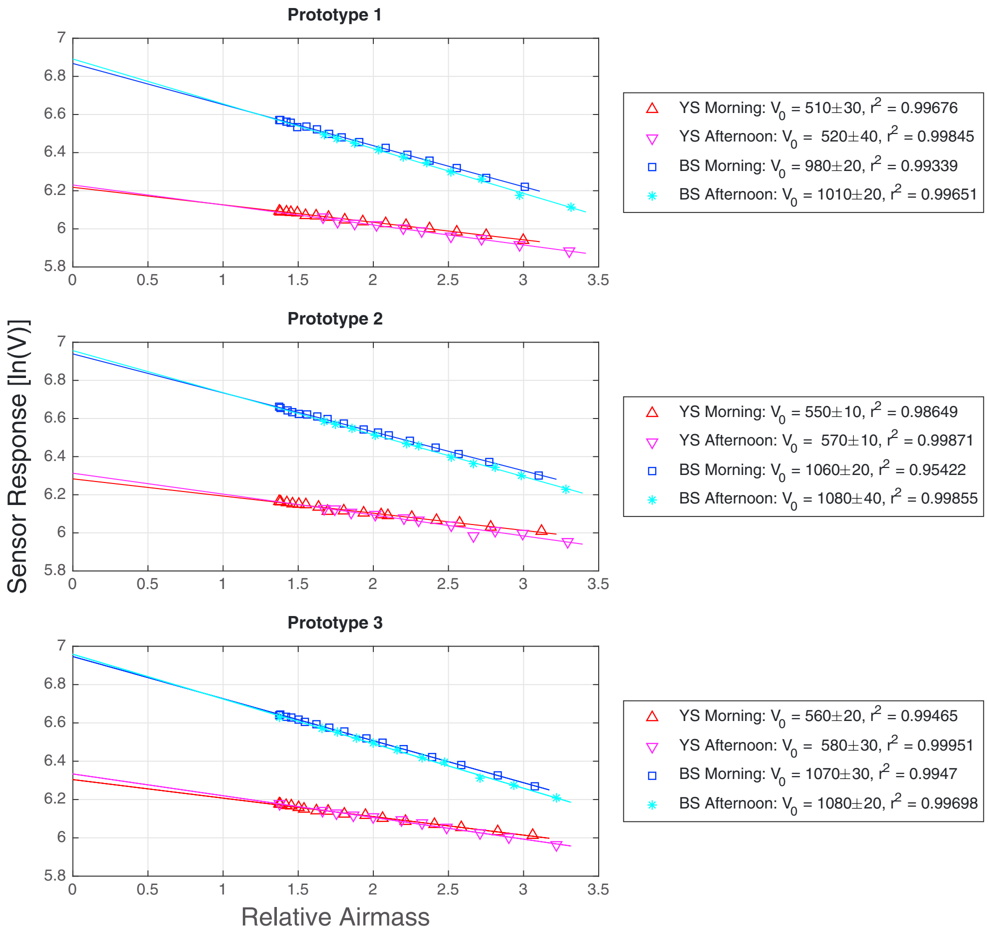

Figure 6. Langley plots for the yellow (YS) and blue (BS) sensors for the three prototypes, showing the calibration constant V_0 and r^2 obtained in each extrapolation. The results are almost identical to those expected from a monochromatic Langley Plot. Measurements taken on 21 May 2016, at the Chajnantor Plateau of the Atacama Desert, Chile (4500 m asl).

(equation (6)) and the AOT of the closest CIMEL channels, centered at 440, 500, and 675 nm. Here τ_λ is the optical thickness at wavelength λ, τ_{λ_0} is the optical thickness at the reference wavelength τ_{λ_0}, and α is the Ångström coefficient.

$$\frac{\tau_\lambda}{\tau_{\lambda_0}} = \left(\frac{\lambda}{\lambda_0}\right)^{-\alpha} \tag{6}$$

The parameter α is calculated using CIMEL AOT measurements for two different wavelengths λ_1 and λ_2 (channels 380 and 440 nm for the blue sensor, and 500 and 675 nm for the yellow one).

$$\alpha = -\frac{\log_{10}\left(\frac{\tau_{\lambda_1}}{\tau_{\lambda_2}}\right)}{\log_{10}\left(\frac{\lambda_1}{\lambda_2}\right)} \tag{7}$$

Weather conditions allowed three almost full clear days for these calibration measurements, on 6, 7, and 10 June 2016. To provide the possibility of testing the adjustment with independent measurements, it is decided to use the data of 6 and 10 June to calculate the bias correction coefficients and the data of 7 June to compare the corrected measurements with the CIMEL. This is done because the 6 and 10 June data provided a large span of AOT values for the city of Santiago, between 0.1 and 0.4 for the 500 nm channel and the day 7 also shows a large dynamic range on its own (AOT at 500 nm between 0.15 and 0.27 approximately) (Escribano et al., 2014).

Table 2
Yellow Sensor, Bias Correction Coefficients Before and After the Campaigns (Calibration and Validation Columns, Respectively) and Their Variation

	Calibration		Recalibration		Difference (%)	Difference (AOT)
Prototype	m	n	m	n	m	n
1	1.019	0.016	1.016	0.001	−0.294	−0.015
2	1.026	−0.001	1.010	0.014	−1.559	0.015
3	1.071	0.012	1.059	−0.055	−1.120	−0.067

A first-grade relationship was tested between the raw prototype AOT τ_p^* and the CIMEL's AOT τ_c, providing a worst case R^2 of 0.9539 (worst fit considering both sensors of all the prototypes). This motivated the use of the linear model of equation (8) to correct the bias between the CIMEL and each prototype. Here *m* and *n* correspond to the bias correction coefficients, while ϵ is a random error term assumed to have a Gaussian distribution with zero mean.

The two bias correction coefficients *m* and *n* are calculated using all the data from the calibration days with a linear regression. With this procedure we retrieved the values shown in the Calibration column of Tables 2 and 3.

$$\tau_p^* = m \cdot \tau_c + n + \epsilon. \tag{8}$$

Then, the bias is removed using equation (9). Here τ_p is the corrected prototype AOT and ϵ' represents the corrected measurement random error. Figure 7 shows the measurements of the corrected prototype versus the CIMEL for the validation day. Here it is possible to see a good agreement between the prototypes and the CIMEL, especially in the capture of the variability of aerosols.

$$\tau_p = \frac{\tau_p^* - n}{m} + \epsilon' \tag{9}$$

Since this bias correction may change over time, after all the measurement campaigns, a recalibration is carried out using the same procedure on 6 July 2016. The Recalibration column of Tables 2 and 3 show the after-campaign bias correction coefficients. By doing this procedure it is possible to detect a possible erratic functioning of any prototype. For instance, prototype 1 in Table 3 shows a 7% difference in the *m* parameter which might indicate a problem. Since the change seems to be limited, we prefer to assume a linear change of the parameters over time. This consists on using the calibration *m* and *n* parameters for the early stage of the campaign, and then interpolate these values in a linear manner with respect to time to reach the final *m* and *n* values retrieved in the recalibration. This is done to reduce as much as possible the introduction of bias in the measurements; however, a clear criteria to decide between correcting and discarding the data has to be studied.

After removing the bias, we can use the same testing data set to calculate an approximation of the standard deviation introduced by the random error ϵ' to quantify the instrument accuracy. To do this we use the root-mean-square error (RMSE) (equation (10)) assuming the CIMEL value as the ground truth. All the prototypes measurements, τ_{pi}, are included in the data pool, obtaining $N = 78$ samples, with the objective of calculating

Table 3
Blue Sensor, Bias Correction Coefficients Before and After the Campaigns (Calibration and Validation Columns, Respectively) and Their Variation

	Calibration		Recalibration		Difference (%)	Difference (AOT)
Prototype	m	n	m	n	m	n
1	1.004	0.021	1.119	−0.017	11.45	−0.038
2	0.986	0.003	1.080	0.001	9.533	−0.002
3	1.025	0.022	1.026	−0.050	0.098	−0.072

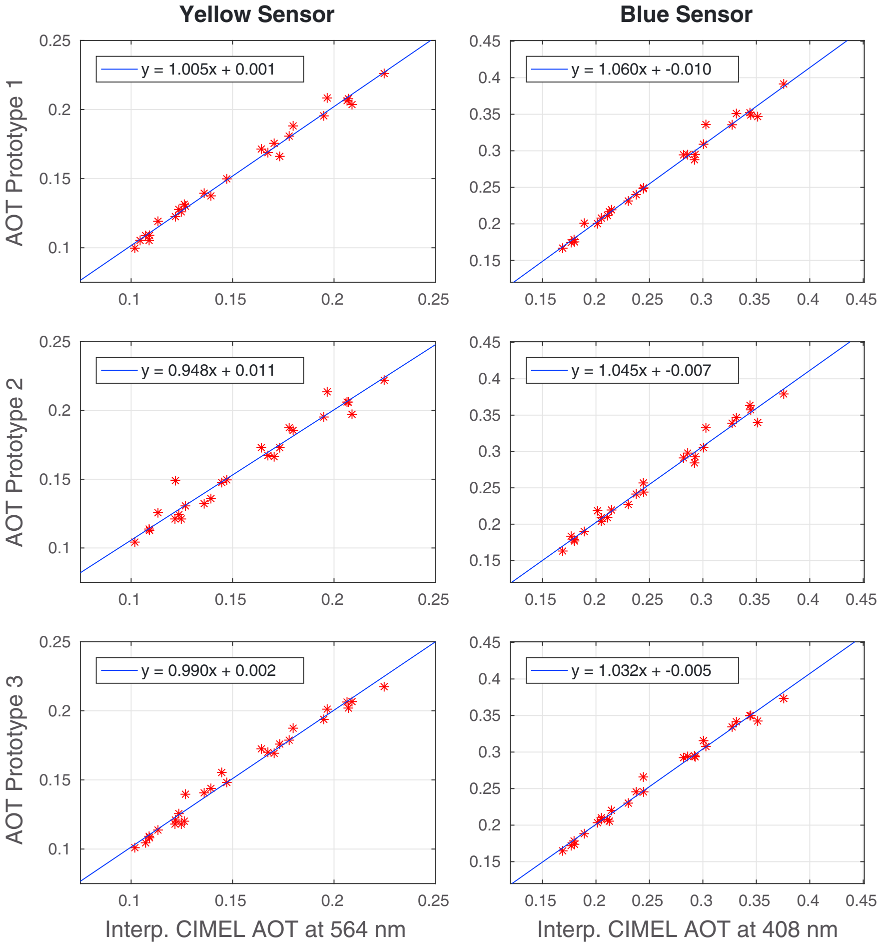

Figure 7. Bias-corrected measurements of the (a) yellow and (b) blue channels compared to their CIMEL equivalent AOT. Measurements taken on 7 June 2016.

the RMSE that our LED Sun photometers have in average. After the calculations we obtained a RMSE of $\sigma_y = 0.006$ for the yellow sensor and $\sigma_b = 0.009$ for the blue sensor.

$$\text{RMSE} = \sqrt{\frac{\sum_{i=1}^{N}(\tau_{\text{ci}} - \tau_{\text{pi}})^2}{N}} \tag{10}$$

Finally, a histogram using the same data set of the RMSE calculation is included in Figure 8 to illustrate the behavior of the prototype samples after the bias corrections. It reflects that in most cases the percentage error is below the 10%, which is significantly lower than the uncertainty obtained with satellite products such as MAIAC (close to 50% for urban areas) (Martins et al., 2017).

5. Distributed Measurements

One of the main goals of the development of low-cost Sun photometers is to increase the AOT spatial coverage within a small region without resorting to increase the number of CIMEL- like instruments. To do this, an important constraint is to obtain a low uncertainty in the measurements.

Therefore, to keep the instruments calibrated and their uncertainty characterized, we developed a procedure for calibration and correction of the measurements that relies on satellite data and takes advantage of the existing CIMEL Sun photometer instrument at the DGF of the University of Chile, Santiago.

In this section we present the results of two small field campaigns conducted to test the accuracy of our prototypes and the urban-sized network concept. In total we used the three built prototypes, a CIMEL and a MICROTOPS II handheld Sun photometer to increase the spatial coverage possibilities.

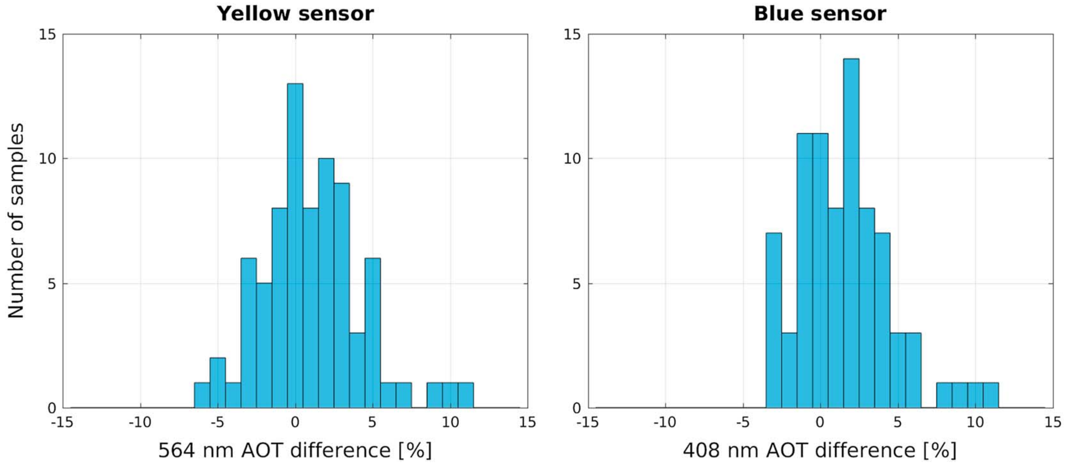

Figure 8. Percentage error with respect to the CIMEL considering the *N* AOT samples obtained in the validation with the three prototypes. Percentage error calculated as $100(\tau_p - \tau_c)/\tau_c$.

The first campaign was performed inside the Santiago basin with the objective of studying the AOT variability in urban-sized scales. In the second campaign we distributed the instruments along a mountain road nearby Santiago. Before both campaigns, the prototypes were calibrated using the procedure of section 4. The MICROTOPS II Sun photometer was operated using the manufacturer's calibration.

5.1. First Campaign

The first campaign was carried out in 11 June 2016. The observation points were located in the DGF, San Joaquin and La Reina, shown in Figure 9. The prototype at the DGF site was operated alongside the CIMEL and MICROTOPS II Sun photometers.

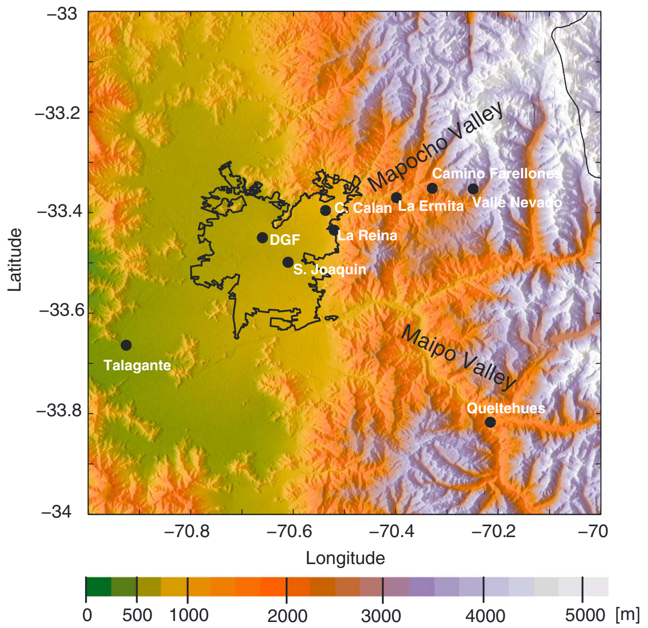

Figure 9. Map showing the area studied in the field campaigns. The black line shows the limits of the urban area of Santiago, with the ground altitude indicated by the color scale. The location of the Sun photometers and other stations is indicated by black dots. The sites involved in the first campaign are the DGF, San Joaquin, and La Reina, while in the second campaign the observation points were alternating between the DGF, Cerro Calan, La Ermita, Camino Farellones, Valle Nevado, and Talagante. Additionally, Queltehues location is indicated to reference a previous study (Cordova et al., 2016).

A remarkable first result of this experiment is the behavior of the MODTRAN AOT correction (see equations (4) and (5)). Figure 10 shows the measured AOT at the wavelength of 564 nm of the three photometers located at DGF, which includes one of our prototypes alongside the commercial Sun photometers CIMEL and MICROTOPS II. Figure 10 presents the result of the measurement before and after correcting for the ozone and water vapor effect, enabling a better appreciation of the influence of each atmospheric component.

Furthermore, it shows that the prototype closely follows the AOT behavior observed by the CIMEL, and since the observed changes are larger than the measurement uncertainty (see section 4.2), it proves that AOT can have significant daily cycle variations for close points (for example, the DGF and La Reina sites are separated by roughly 13 km).

Even if we put aside the absolute accuracy of the retrieved AOT value, the change of AOT over time is well captured by the prototype instruments, even without corrections. This feature by itself would allow the study of the AOT dynamics in an urban-sized region, provided a large enough number of sensors.

Figure 11 shows the measured AOT time series for the two channels at all the locations of this campaign. We observe maximum AOT near 17 UTC (13 local time) in DGF and a later maximum in the San Joaquin and La Reina locations. These particular results are consistent with the increase of concentrations of aerosols due to morning time emissions near downtown, which are later transported by the valley mountain circulations during the afternoon (Schmitz, 2005). Available data from MAIAC product (Lyapustin et al., 2011) during two MODIS overpasses

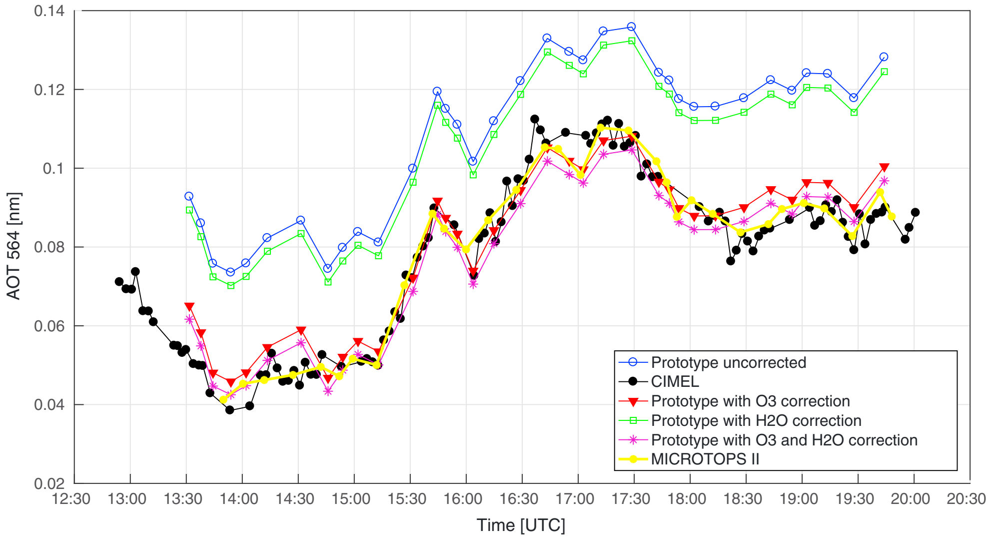
Corrected yellow sensor measurements 11/06/2016
GOT estimated using MODTRAN

Figure 10. Yellow sensor measurements before and after gases correction. One of the prototypes was located at the rooftop of the DGF, next to a CIMEL and a commercial handheld Sun photometer MICROTOPS II. The ozone correction is significantly more important in the AOT estimation compared to the water vapor effect using this yellow sensor.

(a) Yellow Sensor AOT Measurements 11/06/2016

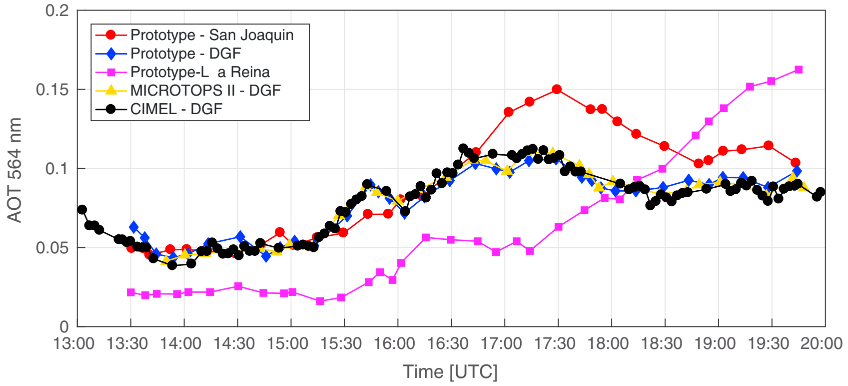

(b) Blue Sensor AOT Measurements 11/06/2016

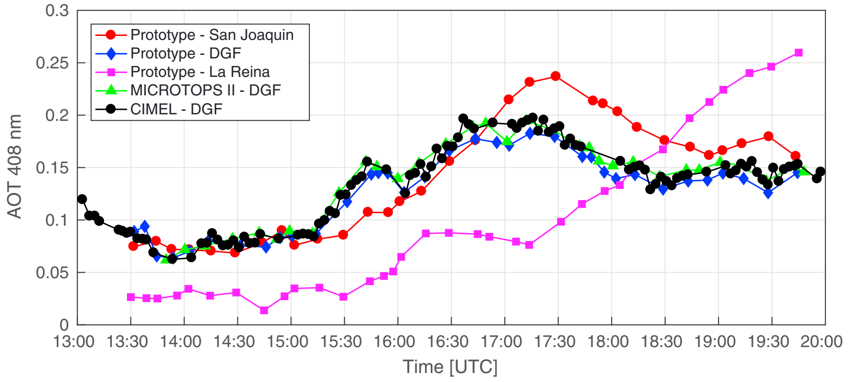

Figure 11. Measurements of AOT from the yellow and blue obtained in the first campaign. They represent simultaneous AOT results obtained at different observation points distributed within Santiago basin. The three built prototypes, one CIMEL and one MICROTOPS II were used.

(Figure 12), show similar values of AOT at 550 nm, in particular, a widespread increase of AOT from about 15 UTC to 18 UTC over the city and also a spatial distribution of AOT, which is consistent with the one found by the surface instruments. The satellite product confirms the sharp spatial variability of AOT at the urban scale, which is hardly captured by a single AOT measurement.

(a) AOD 550 nm June 6th 2016 15:15 UTC

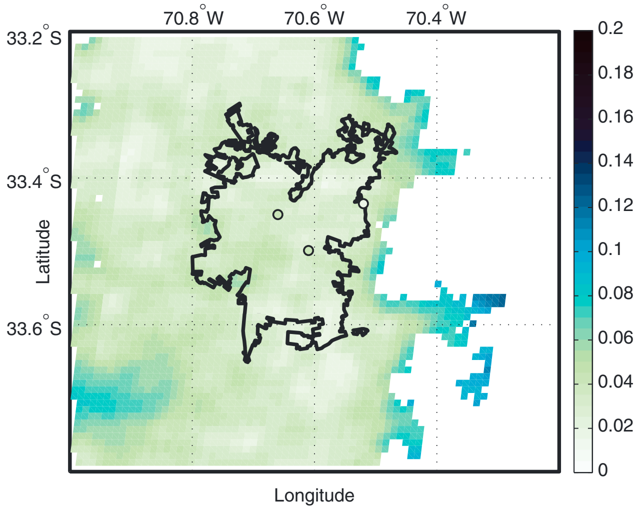

(b) AOD 550 nm June 6th 2016 17:55 UTC

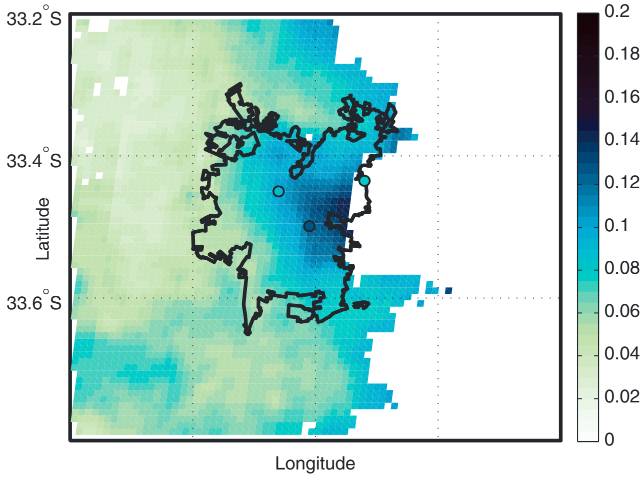

Figure 12. Satellite retrievals of AOT at 550 nm from the MAIAC product (Lyapustin et al., 2011) over the Santiago Region. The black edge dots indicate the values of the AOT measured by the Sun photometers and taken to 550 nm using both Yellow and Blue Chanel measurements. (a) 6 June 2016, 15:15 UTC and (b) 6 June 2016 17:55 UTC.

5.2. Second Campaign

Motivation for a second campaign is provided by the possible transport of urban-emitted aerosols to the Andes and the ultimate fate of these aerosols. Southwesterly breeze over Santiago (as shown in Schmitz, 2005) develops during the afternoon in response to diurnal orographic heating, potentially carrying pollutants emitted downtown along the Mapocho Valley in the northeast of the city (see Figure 9). Although the fate of these aerosols is currently unknown, there is a potential for aerosols and black carbon to reach the high Andes and deposit over snow and ice surfaces. For instance, Cordova et al. (2016) studied the arrival of aerosols to a site located at around 1,500 m above mean sea level in El Maipo basin (Queltehues in Figure 9) finding an increase in aerosols during the afternoon restricted to clear sky days. The valley studied by Cordova et al. (2016) was found not to be strongly affected by transport from the city rather than from emissions in the rural locations along the Maipo Valley. Given the diurnal circulation in Santiago, a more direct influence by the city is expected along the Mapocho basin (see Figure 9). This thermally driven transport has been hypothesized to be a relevant component of the increased rate of glaciers melting (Molina et al., 2015), as suggested by studies in other places around the world (Lau et al., 2010).

The observation points of the second campaign were distributed along one of the main access routes to the Andes, Camino Farellones along the Mapocho River basin (see Figure 9). Since clear sky conditions are required to obtain Sun photometer measurements, the campaign was distributed in 3 days, the 16, 18, and 28 June 2016. In addition to our three prototypes we also used one MICROTOPS II and the CIMEL of the DGF. Each measurement point location is shown in Figure 9.

Figures 13–15 show the AOT for both channels at each day of campaign. The prototypes and CIMEL Sun photometer were used in the same location for all the campaign days, and the MICROTOPS II was moved from Talagante to Cerro Calan.

The results for 16 June can be seen in Figure 13. Data show almost no diurnal cycle within the Santiago basin and similarly in the high-altitude stations. AOT decreases monotonically with altitude, which is consistent with stable conditions and emissions mostly restricted to the city. Assuming that the measurements at Valle Nevado are representative of other points at similar altitude, we can conclude that there was not a significant aerosol presence over 3,000 m asl for that day.

It is also worth discussing the high AOT value measured at Talagante during the whole day. This might be caused by the use of wood stoves that are widespread in rural parts of southwest Santiago. The AOT decrease in Talagante at 17 UTC coincides with an increase of AOT at the DGF. This might be caused by transport of the aerosols produced by the wood combustion in rural areas into the city, which happens to be a wood stove forbidden zone. A hint of these emissions can be seen in Figure 12 where Talagante is located in the lower left grid cell of the map. Cordova et al. (2016) attributed their observation of transport into the mountain region of the Maipo basin to transport from these rural areas.

(a) Yellow Sensor AOT Measurements 16/06/2016

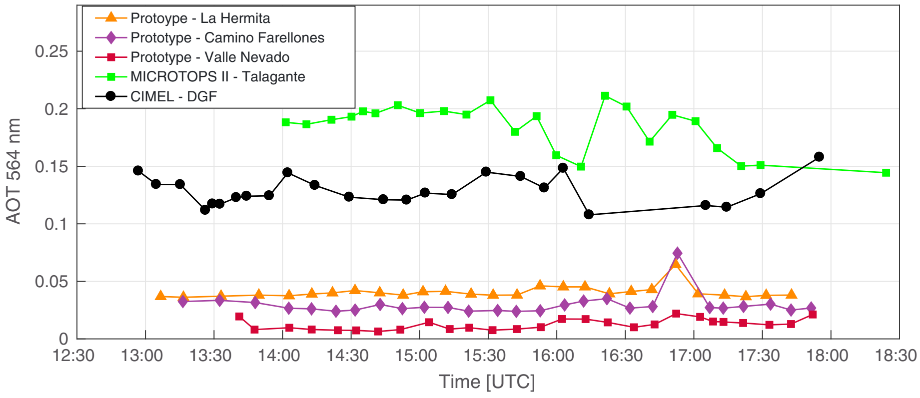

(b) Blue Sensor AOT Measurements 16/06/2016

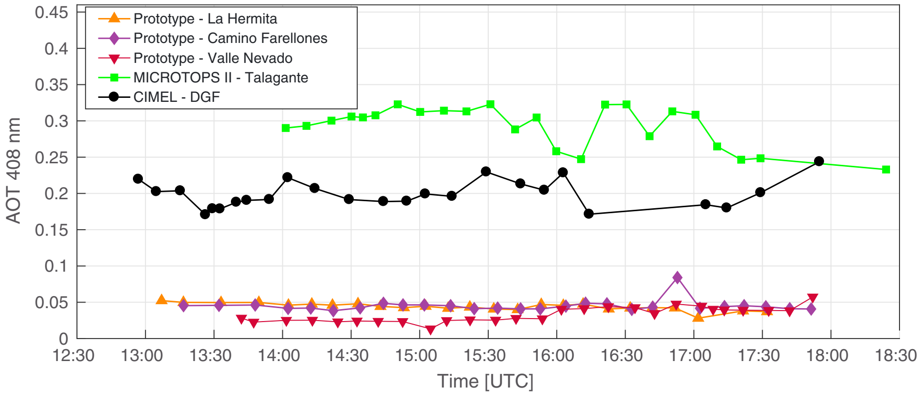

Figure 13. Measurements of AOT for 16 June 2016. Location and altitude of the instruments: Talagante: 326 m asl, DGF: 500 m asl, La Ermita: 1165 m asl, Camino Farellones 1974 m asl, and Valle Nevado: 3033 m asl.

Since no evidence of AOT increment is seen over 1,500 m asl (La Ermita, Camino Farellones, and Valle Nevado) before the time of sunset, we decided to move the Sun photometer (MICROTOPS II) from Talagante to Cerro Calan. This point is near the entrance to the Mapocho Valley but still within the city. The DGF and Cerro Calan sites are aligned, and therefore they are useful to check if there is a smaller-scale flow of aerosols into the mountains, with the added advantage of increasing the aerosol tracing capability for circulation coming from the east.

Figure 14 shows the AOT measured during 18 June. In this day, the data shows a small decrease of AOT in the mountain stations during the morning. Meanwhile, AOT is relatively stable at DGF place (downtown). However, at 16:30 UTC AOT clearly rises at Cerro Calan, followed by a slight increment in La Ermita and no evidence of increment at higher points.

Our interpretation for the AOT results during this particular day is that only a weak upslope transport occurred under very stable atmospheric conditions but only reaching about 1,000 m. An increase in AOT at Cerro Calan (and to some extent at La Ermita) at the foothills of the Andes is further evidence of this transport. AOT in the mountains seem to behave similarly to 16 June, with even lower values at Valle Nevado. In fact, the low AOT concentrations have a magnitude close to the prototypes uncertainty, and therefore, even negative values of AOT are observed. AOT at Cerro Calan continues increasing until sunset therefore suggesting the possibility of further increases during the evening due to transport from downtown locations. Mountain sites appear mostly uncoupled from the AOT behavior within the city.

The final campaign day was 28 June. AOT data are shown in Figure 15. During this day the AOT behavior was significantly more dynamic. AOT increases downtown (DGF) after 15 UTC, reaching a peak value at 17:30 UTC,

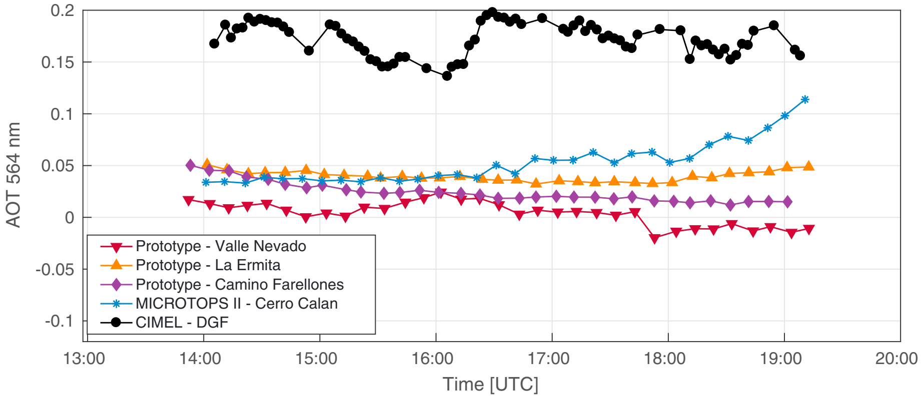
(a) Yellow Sensor AOT Measurements 18/06/2016

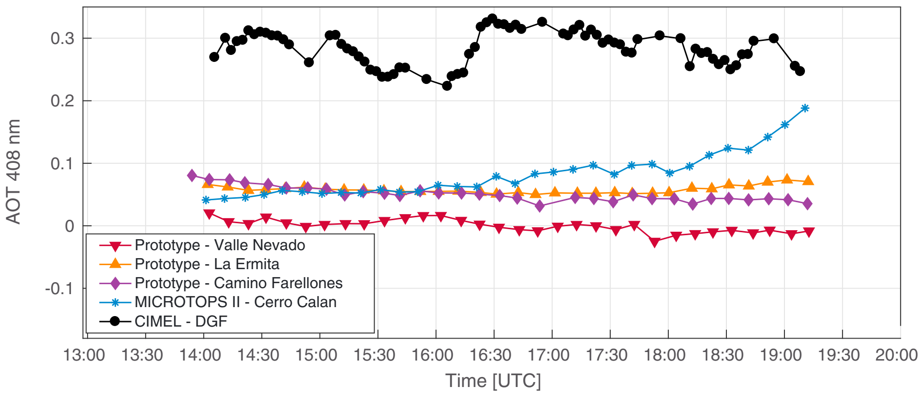
(b) Blue Sensor AOT Measurements 18/06/2016

Figure 14. Measurements of AOT for 18 June 2016. Location and altitude of the instruments: DGF: 500 m asl, Cerro Calan: 867 m asl, La Ermita: 1165 m asl, Camino Farellones 1974 m asl, and Valle Nevado: 3033 m asl.

and then starts to decrease. On the other hand, at Cerro Calan, nearly 1,000 m asl of altitude, the measurements increase continuously over time almost doubling by the end of the day. At Valle Nevado, over 3,000 m asl, we see similar increment of AOT than that at DGF, but the increment starts 1 h before and the decrease 1.5 h before. The peak value is not negligible reaching 0.07 of optical thickness for the blue sensor. This value is higher than some samples registered under the 1,000 m of altitude. Camino Farellones, at 2,000 m of altitude, follows a different trend that the other points, decreasing almost constantly since the 14 h UTC.

One can speculate that the aerosols originally located at Camino Farellones (perhaps an elevated layer caused by the circulation on the previous day, e.g., Muñoz & Alcafuz, 2012) are transported upslope to Valle Nevado, decreasing locally while increasing at Valle Nevado. Further decreases at Valle Nevado later in the afternoon take the AOT values close to background values (~0.01 in the yellow sensor).

We reckon that proposed explanations of the data we present above are at most tentative, especially given the small number of points and short time span of measurements. However, rather than proposing full explanations for the AOT behavior over complex terrain around Santiago, we want to highlight the rich behavior of AOT over short spatial scales, which justifies studies with a much larger number of sensors for extended periods of time. Only by using low-cost instrumentation, high-density spatial coverage becomes feasible. The procedure indicated in this work would enable the intercomparison of these relatively low-precision sensors using a reference instrument, such as a CIMEL, with an uncertainty below the actual AOT variations observed within small distances.

(a) Yellow Sensor AOT Measurements 28/06/2016

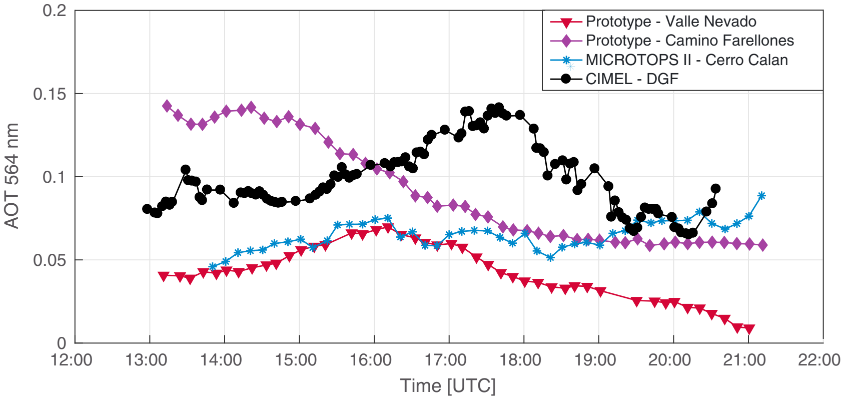

(b) Blue Sensor AOT Measurements 28/06/2016

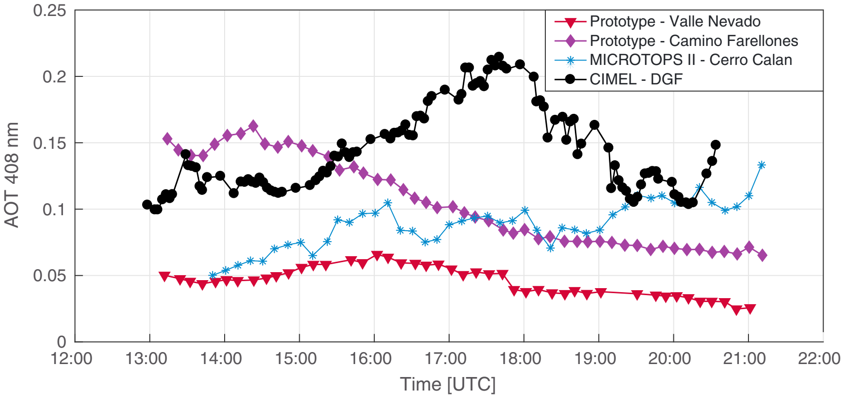

Figure 15. Measurements of AOT for 28 June 2016. Location and altitude of the instruments: DGF: 500 m asl, Cerro Calan: 867 m asl, Camino Farellones 1974 m asl, and Valle Nevado: 3033 m asl. Only two prototypes were operative this day.

6. Discussion and Conclusions

This work is motivated by the hypothesis that the AOT dynamics is rich inside metropolitan areas. This hypothesis is supported by satellite products such as MAIAC, which achieves a spatial resolution of 1 km. However, the accuracy of these measurements is still poor within metropolitan areas due to variability of the reflectivity inside them and also provide a low temporal resolution due to few passes per day. This seriously restricts the use of space-based instruments in the study of complex AOT dynamics inside cities. Besides, the measurements and the spatial resolution of satellites need to be validated and calibrated using ground measurements.

The aforementioned facts and the results of our campaigns justify the necessity of measuring AOT with a much denser Sun photometer network, with an average separation between instruments under 10 km. Currently, many major cities have CIMEL Sun photometers to study AOT. Data measured by these instruments are collected in a global network, the AERONET. Nevertheless, the cost of these precise autonomous instruments makes prohibitive, especially for developing countries, their use in large numbers at metropolitan scales to increase the AOT spatial resolution.

Other type of Sun photometers were proposed in the early 1990s based on inexpensive light-emitting diodes. However, these inexpensive photometers have limitations in their accuracy, reliability, and fidelity. The low-cost LED-based Sun photometers have been used at large spatial scales in a network called GLOBE. In this work we propose that these LED-based Sun photometers might be more useful by avoiding the competition with the AERONET network that arises from measuring aerosols at continental (or global) scales, and rather focus on their application of characterizing the AOT behavior at small scales, specifically in metropolitan areas taking advantage of the AERONET instruments.

We demonstrated in this work that the performance of these inexpensive Sun photometers can be improved by modeling the sensor behavior and including corrections based on data comparison with an accurate CIMEL Sun photometer. With this procedure the LED-based Sun photometers can provide much more valuable, precise, and reliable information about the AOT dynamics in city areas. In addition, we propose our LED-based Sun photometer as instruments with an open hardware/software and calibration standard. This enables the scientific community the evaluation of our methodology to estimate AOT, and most important, it allows intercomparison measurements not only between instruments but also between different periods of time and changes or improvements of the instrument.

In this work it was shown that LEDs Sun photometer are a suitable alternative for high-density aerosol monitoring networks. The low cost of each instrument (~150 USD) allows for the deployment of tens of measurement points within a single city or point of interest, the higher cost being the labor of the operators. However, the lower cost of the sensors introduces new challenges that high-grade photometers do not have. The AOT estimation becomes harder because of the wider spectral response of LEDs, which imposes the need for correcting the effects of atmospheric gases in the measurements and also introduces a systematic error in the AOT estimation due to the use of the monochromatic Beer-Lambert model.

To reduce the effect of these error sources, we implemented an improvement in the LED-based Sun photometer calibration and operation. For calibration, a Langley Plot is first used to estimate the inversion model calibration constant and then the measurements are corrected using a side by side calibration with a CIMEL. After these calibrations the low-cost Sun photometers are ready to measure and be deployed on terrain to gather data. The gases effect introduced in the measurements by the wide sensors response is corrected by MODTRAN simulations of the GOT using O_3 and H_2O columns estimated by satellite and ground instrumentation. After the measurement campaign, a second side by side calibration with CIMEL is performed to check for possible drift of the instruments while on the field. The correction terms are then interpolated over time and used to correct the bias of the field measurements. This method also enables the intercomparison of all the instruments with a common reference.

The estimated uncertainty with respect to the CIMEL for the prototype is of 0.006 for the 564 nm channel and of 0.009 for the one at 408 nm in the AOT range used for calibration validation. These values are below the observed variability within short distances, showing the capability of the low-cost Sun photometers to register the aerosol variability, improving the data available for high-resolution chemical transport modeling. Additionally, the estimated error is below that of high-resolution satellite products in cities (Martins et al., 2017). Therefore, a network of such low-cost Sun photometers could provide high-quality data for satellite validation and correction.

A proof of concept AOT monitoring network of three-instrument prototypes plus a CIMEL and a MICROTOPS II Sun photometer allowed us to unveil radically different daily cycles for locations separated by less than 15 km. During the campaign period we had a day where we measured significant AOT values at 3,000 m asl altitude in Valle Nevado, which suggest the possibility that aerosols emitted from the city are effectively reaching glacier altitude (above 4,500 m at Santiago latitude). Determining the source of these aerosols could also be done using a distributed network of instruments in the area, together with high-resolution chemical transport modeling. The advantage of this method over surface particle counter networks are mainly the increased tolerance to local emissions sources and the possibility of detecting larger-scale atmospheric behavior given the nature of AOT that takes into account all aerosols in the air column.

These results allow us to envision the potential information that high-density AOT monitoring networks could provide for model validation, pollution dispersion research, and satellite data correction, among others. However, some limitations of the present method could be potentially improved. First, an automatic Sun tracking prototype that maintains a similar cost is desired to ease the acquirement of extensive time series data and the cost of labor. This requirement and the campaign results also imply that more stress should be put on the instruments reliability for future designs. Regarding the correction of the effect of atmospheric gases on the retrieval, spectral radiative modeling by MODTRAN proved a useful tool. Additional LED sensors in other channels could enable the measurement of gases alongside AOT, even allowing the possibility of automatically correcting the GOT effect without the need of supplementary gases data and a more accurate estimation of Ångström coefficient and other aerosol optical properties. Finally, we have illustrated with a few days of field measurements that AOT daily cycle of nearby sites can have large differences both in magnitude and amplitude. Because of this, the uncertainty of the instrument with respect to the CIMEL must be studied for a more extended period of time to capture a broader AOT range, reducing the expected error for a larger span of AOT values.

Acknowledgments
These research has received financing from the Center for Climate and Resilience Research, the Space and Planetary Exploration Laboratory, the consultant Meteodata, the Fondecyt Regulares 1151125 and 1151476, the CONICYT-ANILLOS ACT1410 and ACT1405, and the grant CONICYT-PFCHA/MagísterNacional/2017-22171420. This work would have been impossible without the support from these institutions, and therefore, we are sincerely thankful for their help. We would also like to acknowledge the Laboratory of Photoacoustics and Photothermic Phenomena of the Department of Physics and Center of Optics and Photonics (CEFOP) at the University of Concepción, the company Ingeniería MCI Ltda., the FABLAB of the University of Chile, and the students Ignacio Becker and Guillermo Cruz for their help in the prototypes construction and characterization. Finally, we thank Alejandra Molina and Mirko del Hoyo for their logistical assistance in the field campaigns. Marcos Diaz would like to thank the Editor Zhanqing Li and the two anonymous reviewers for their assistance in evaluating this paper. The resources required to build this instrument can be found in https://github.com/FelipeToledo/DIY-SunPhotometer-UChile. Comments are welcome!

References

Berk, A., Anderson, G. P., Acharya, P. K., Bernstein, L. S., Muratov, L., Lee, J., … Shettle, E. P. (2006). Modtran5: 2006 update. *Algorithms and Technologies for Multispectral, Hyperspectral, and Ultraspectral Imagery*, *XII*, 62331F. https://doi.org/10.1117/12.665077

Brooks, D. R. (2008). *Bringing the Sun down to Earth: Designing inexpensive instruments for monitoring the atmosphere*. Dordrecht; London: Springer Science & Business Media.

Brooks, D. R., & Mims, F. M. (2001). Development of an inexpensive handheld LED-based Sun photometer for the globe program. *Journal of Geophysical Research*, *105*, 4733–4740.

Bucholtz, A. (1995). Rayleigh-scattering calculations for the terrestrial atmosphere. *Applied Optics*, *34*(15), 2765–2773. https://doi.org/10.1364/AO.34.002765

Butler, D. M., & MacGregor, I. D. (2003). Globe: Science and education. *Journal of Geoscience Education*, *51*(1), 9–20.

Cordova, A. M., Arévalo, J., Marín, J. C., Baumgardner, D., Raga, G. B., Pozo, D., … Rondanelli, R. (2016). On the transport of urban pollution in an Andean mountain valley. *Aerosol and Air Quality Research*, *16*, 593–605.

Dee, D. P., Uppala, S. M., Simmons, A. J., Berrisford, P., Poli, P., Kobayashi, S., … Vitart, F. (2011). The ERA-Interim reanalysis: Configuration and performance of the data assimilation system. *Quarterly Journal of the Royal Meteorological Society*, *137*(656), 553–597. https://doi.org/10.1002/qj.828

Escribano, J., Gallardo, L., Rondanelli, R., & Choi, Y. S. (2014). Satellite retrievals of aerosol optical depth over a subtropical urban area: The role of stratification and surface reflectance. *Aerosol and Air Quality Research*, *14*, 596–607. https://doi.org/10.4209/aaqr.2013.03.0082

Hauser, P. C., Rupasinghe, T. W., & Cates, N. E. (1995). A multi-wavelength photometer based on light-emitting diodes. *Talanta*, *42*(4), 605–612.

Holben, B. N., Eck, T., Slutsker, I., Tanre, D., Buis, J., Setzer, A., … Smirnov, A. (1998). Aeronet—A federated instrument network and data archive for aerosol characterization. *Remote Sensing of Environment*, *66*(1), 1–16.

Lau, W. K. M., Kim, M.-K., Kim, K.-M., & Lee, W.-S. (2010). Enhanced surface warming and accelerated snow melt in the Himalayas and Tibetan Plateau induced by absorbing aerosols. *Environmental Research Letters*, *5*(2), 25204.

Li, S., Kahn, R., Chin, M., Garay, M., & Liu, Y. (2015). Improving satellite-retrieved aerosol micro physical properties using GOCART data. *Atmospheric Measurement Techniques*, *8*(3), 1157–1171.

Lyapustin, A., Wang, Y., Laszlo, I., Kahn, R., Korkin, S., Remer, L., … Reid, J. S. (2011). Multiangle implementation of atmospheric correction (MAIAC): 2. Aerosol algorithm. *Journal of Geophysical Research*, *116*, D03211. https://doi.org/10.1029/2010JD014986

Martins, V. S., Lyapustin, A., de Carvalho, L. A. S., Barbosa, C. C. F., & Novo, E. M. L. M. (2017). Validation of high-resolution MAIAC aerosol product over South America. *Journal of Geophysical Research: Atmospheres*, *122*, 7537–7559. https://doi.org/10.1002/2016JD026301

Mims III, F. M. (1992). Sun photometer with light-emitting diodes as spectrally selective detectors. *Applied Optics*, *31*, 6965–6967.

Molina, L. T., Gallardo, L., Andrade, M., Baumgardner, D., Borbor-Córdova, M., Bórquez, R., … Schwarz, J. P. (2015). Pollution and its impacts on the South American cryosphere. *Earth's Future*, *3*(12), 345–369.

Muñoz, R. C., & Alcafuz, R. I. (2012). Variability of urban aerosols over Santiago, Chile: Comparison of surface PM10 concentrations and remote sensing with ceilometer and lidar. *Aerosol and Air Quality Research*, *12*(1), 8–19.

NASA (1976). *U.S. standard atmosphere supplements*. Washington, DC: U.S Government Printing Office.

Schmitz, R. (2005). Modelling of air pollution dispersion in Santiago de Chile. *Atmospheric Environment*, *39*(11), 2035–2047. https://doi.org/10.1016/j.atmosenv.2004.12.033

Stratasys (2015). ABSplus-P430 production-grade thermoplastic for design series 3D printers. datasheet of the ABS thermoplastic.

Stratasys (2017). PLA economy thermoplastic for stratasys F123 series printers. datasheet of the PLA thermoplastic.

Superczynski, S. D., Kondragunta, S., & Lyapustin, A. I. (2017). Evaluation of the multi-angle implementation of atmospheric correction (MAIAC) aerosol algorithm through intercomparison with VIIRS aerosol products and AERONET. *Journal of Geophysical Research: Atmospheres*, *122*, 3005–3022. https://doi.org/10.1002/2016JD025720

Volz, F. (1959). Photometer mit selen-photoelement zur spektralen messung der sonnenstrahlung und zur bestimmung der wellenlängenabhängigkeit der dunsttrübung. *Archiv für Meteorologie, Geophysik und Bioklimatologie, Serie B*, *10*(1), 100–131.

Wallace, J. M., & Hobbs, P. V. (2006). *Atmospheric science: An introductory survey*. Burlington, MA: Academic Press, 92.

Wang, Y., Xin, J., Li, Z., Wang, S., Wang, P., Hao, W. M., … Sun, Y. (2011). Seasonal variations in aerosol optical properties over China. *Journal of Geophysical Research*, *116*, D18209. https://doi.org/10.1029/2010JD015376

Weissert, L., Salmond, J., Miskell, G., Alavi, M., Grange, S., Henshaw, G. S., & Williams, D. E. (2017). Use of a dense monitoring network of low-cost instruments to observe local changes in the diurnal ozone cycles as marine air passes over a geographically isolated urban centre. *Science of The Total Environment*, *575*, 67–78.

Xin, J., Wang, Y., Li, Z., Wang, P., Hao, W. M., Nordgren, B. L., … Hu, B. (2007). Aerosol optical depth (AOD) and Ångström exponent of aerosols observed by the Chinese Sun Hazemeter Network from August 2004 to September 2005. *Journal of Geophysical Research*, *112*, D05203. https://doi.org/10.1029/2006JD007075